

Article

Atmospheric Density Response to a Severe Magnetic Storm Detected by the 520 km Altitude Spherical Satellite

Xinyue Wang^{1,2,3,4}, Yujiao Jin^{1,2,3,4}, Xiangguang Meng^{1,2,3,4,*}, Dan Du⁵, Aibing Zhang^{1,2,3,4}, Xinchun Tang⁶, Feng Yan⁶, Yueqiang Sun^{1,2,3,4}, Xianguo Zhang^{1,2,3,4}, Bowen Wang^{1,2,3,4} and Yuerong Cai^{1,2,3,4}

- ¹ National Space Science Center, Chinese Academy of Sciences, Beijing 100190, China
² Beijing Key Laboratory of Space Environment Exploration, National Space Science Center, Beijing 100190, China
³ Key Laboratory of Science and Technology on Space Environmental Situation Awareness, Chinese Academy of Sciences, Beijing 100190, China
⁴ University of Chinese Academy of Sciences, Beijing 100190, China
⁵ Key Laboratory of Space Weather, National Satellite Meteorological Center (National Center for Space Weather), China Meteorological Administration, Beijing 100081, China
⁶ Shenzhen Aerospace Dongfanghong Satellite Ltd., Shenzhen 518057, China
* Correspondence: xgmeng@nssc.ac.cn



Citation: Wang, X.; Jin, Y.; Meng, X.; Du, D.; Zhang, A.; Tang, X.; Yan, F.; Sun, Y.; Zhang, X.; Wang, B.; et al. Atmospheric Density Response to a Severe Magnetic Storm Detected by the 520 km Altitude Spherical Satellite. *Atmosphere* **2022**, *13*, 1891. <https://doi.org/10.3390/atmos13111891>

Academic Editors: Stavros Kolios and Nikos Hatzianastassiou

Received: 17 October 2022

Accepted: 8 November 2022

Published: 12 November 2022

Publisher's Note: MDPI stays neutral with regard to jurisdictional claims in published maps and institutional affiliations.

Abstract: The polar-orbiting spherical experimental satellite of China for atmospheric density detection with an altitude of ~520 km was successfully launched on 14 October 2021. Based on the dynamic inversion method for atmospheric density and the precise orbit determination data obtained by its GNSS, we inverted the orbital atmospheric density during the severe geomagnetic storm in early November 2021. In this paper, we compared the atmospheric density data obtained by the spherical satellite with the simulations of the MSISE00 and the DTM, evaluated their error distribution, and analyzed the response of the atmospheric density during the severe geomagnetic storm in the dawn–dusk orbit of 520 km altitude. The properties and the physical processes for the atmospheric density of the time evolutions in different latitudes and the global distributions during the severe geomagnetic storm were obtained. We found that the substantial disturbance enhancement and recovery of the atmospheric density of the dawn–dusk orbit have a close correlation with the geomagnetic indexes Kp and Dst. The elevation extends from the poles to the equator, and the relative variation in two hemispheres demonstrates a bimodal nearly symmetric growth structure. The maximum relative variation of the two hemispheres both occurred in the middle latitude, and, for this case, the enhancement of atmospheric density in the mid-latitude region accounted for a larger proportion. The asymmetry between the northern and southern hemispheres is demonstrated by the fact that the absolute value and absolute change in the southern hemisphere in summer are larger than those in the northern hemisphere, and the bimodal structure of the relative variation is inclined to the northern hemisphere.

Keywords: atmospheric density; atmospheric drag force; spherical satellite; precision orbit data; dynamics inversion method



Copyright: © 2022 by the authors. Licensee MDPI, Basel, Switzerland. This article is an open access article distributed under the terms and conditions of the Creative Commons Attribution (CC BY) license (<https://creativecommons.org/licenses/by/4.0/>).

1. Introduction

The thermosphere is an important region for the operation of low-orbit spacecraft and near-space vehicles. Atmospheric drag in the thermosphere is one of the main perturbative forces for the orbits of low-orbit spacecraft and near-space vehicles, and the calculation error of atmospheric density is now the most significant error source of the orbit prediction of low-orbit spacecraft. The inaccurate calculation of atmospheric drag caused by the inaccuracy of the atmospheric density model is the main factor in the orbit prediction. The calculation error of the atmospheric density model may exceed 100% during geomagnetic storms. Catering to the continuous development of commercial satellites, manned spaceflight, and

near-space environment detection, a high-precision atmospheric density model is urgently required for precise orbit prediction [1,2]. The typical semi-empirical models of atmospheric density commonly applied globally include the CIRA, Jacchia, DTM, and MSIS series, among which the DTM and MSIS series are commonly applied atmospheric density models for spacecraft orbit prediction and related research [3,4]. It is shown in studies that the atmospheric density error calculated by the abovementioned semi-empirical atmospheric density models is usually in the range of 15% to 30%. During the disturbance of the space environment, the atmospheric density error calculated by the models may even reach or exceed 100% [5]. The establishment or refinement of a high-precision thermosphere model requires high-precision, global-coverage, long-duration, and quasi-real-time detection of orbital atmospheric parameters.

The satellite-borne in-situ atmospheric density detection, featuring a global spatial coverage and a long-duration and quasi-real-time measurement, is an important method for obtaining high-precision dynamic data of atmospheric density and improving the accuracy of the atmospheric density model. The in-situ measurement of orbital atmospheric density can be obtained by two methods, i.e., pressure measurement and dynamic inversion. The dynamic inversion method may invert the in-situ atmospheric density value based on the measured drag perturbation acceleration. The drag perturbation acceleration is proportional to the windward area-mass ratio of the satellite and the drag coefficient. The spherical satellite can keep the windward area-mass ratio invariable at different attitudes and can also eliminate the error caused by irregular satellite shape to the drag coefficient. It is therefore the optimal satellite configuration for in-situ detection using the dynamic inversion method.

Early detection of gravitational field on satellites was performed by in-situ detection of atmospheric density with accelerometers, such as the Challenging Minisatellite Payload (CHAMP) and the Gravity Recovery and Climate Experiment (GRACE), which are two of the most representative near-Earth space environment detection missions that have obtained atmospheric density data at altitudes of 300–400 km [6–8]. Considering that the in-situ measurement of atmospheric density by a microsatellite network can achieve long-duration, all-round synchronous coverage of low-orbit space, the method of low-cost microsatellite networking has been gradually adopted globally to detect atmospheric parameters. For example, the low-cost thermosphere exploration mission ANDE 2 (the Atmospheric Neutral Density Experiment 2) proposed by the US Naval Research Laboratory launched two spherical satellites with an orbital altitude of about 350 km in July 2009 to fulfill the goal of monitoring the orbital atmospheric density [9]. QB50, an international collaborative mission sponsored by the European Union, has launched many satellites since 2011 to carry out multi-point in-situ detection of the Earth's lower thermosphere at an altitude of 200–380 km. There have been 38 satellites launched as of 2017 [10,11]. Considering the current status quo of detection and simulation of the atmospheric environment, the in-situ detection of orbital atmospheric parameters by a low-orbit microsatellite network is urgently required for the establishment and refinement of high-precision thermosphere models.

The spherical experimental satellite for measuring atmospheric density, which was jointly developed by the NSSC (National Space Science Center, CAS) and Shenzhen Aerospace Dongfanghong Satellite Ltd. of China Aerospace Science and Technology Corporation, is a pioneer of low-orbit microsatellite networking for in-situ orbital atmospheric density detection, with the goal of carrying out in-situ detection of atmospheric density, obtaining the space-time evolution characteristics and dynamic response mechanism of the orbital atmosphere, and verifying the feasibility of the spherical satellite networking for atmospheric density detection. The spherical satellite was launched into orbit on 14 October 2021, marking the first time that China has carried out in-situ measurement of the atmospheric density of the 520 km polar-orbiting satellite orbit. This paper provides an introduction to the satellite and its GNSS for precise orbit determination, as well as the orbital atmospheric density detection and inversion method. In the third part of this

paper, we compared and analyzed the observation data of atmospheric density with the calculation results of NRLMSISE-00 and DTM models to verify the validity of the scientific data. By analyzing the observed data of atmospheric density during the severe geomagnetic storm, we found the time evolution and global distribution properties at the altitude of 520 km during the severe geomagnetic storm.

2. Instrumentation and Methods

2.1. Spherical Satellite and Orbital Atmospheric Density Detection

The spherical experimental satellite is a microsatellite with a weight of 73.8 kg and a diameter of 800 mm. It operates in a dawn–dusk orbit at an altitude of about 520 km. Its orbital inclination is 97.46° , and its descending node is at around local time 18:00. Its local solar time–latitude motion trajectory is shown in Figure 1b. It is also the first spherical satellite in China that integrates the pressure measurement method and the dynamic inversion method for atmospheric density detection. The main payload of the spherical experimental satellite consists of a pressure-measurement sensor and a GNSS precise orbit-determination payload (GPOD), and was operated after launching to obtain successful data detection.

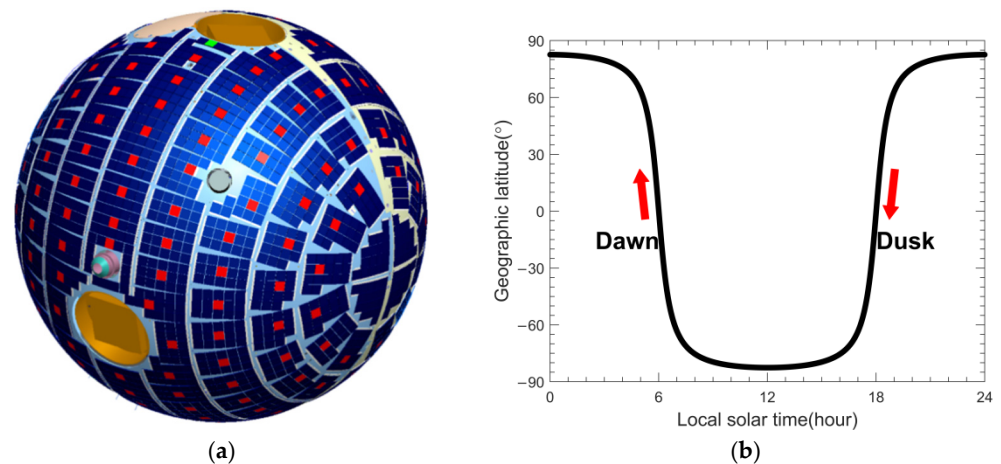


Figure 1. The spherical experimental satellite and its local solar time: (a) the spherical experimental satellite; (b) local solar time and latitude distribution of the satellite orbit.

According to the dynamic inversion method, the in-situ atmospheric density can be inverted from the precise orbit determination data obtained by GPOD [12–14]. The GPOD method can derive the atmospheric density with high precision and resolution, which features consistency compared with measurements [15]. As shown in Figure 1a, the outer surface of the disc-shaped GNSS antenna fits the spherical design of the satellite. The reduced-dynamic POD employed as the routine positioning mode in this study, as well as during periods of geomagnetic disturbance, and the models used in POD procedure can be found in former research [14]. The adoption of both Beidou and GPS precise orbit determination methods contributes to an accuracy of better than 5 cm. See Table 1 for the performances. The inversion of atmospheric density by precise orbit determination has the advantage of self-calibration, requiring no additional calibration. The calculation usually requires the average value of a period of time to gain a higher accuracy. The derived densities are delivered every 30 s. The disadvantage is that the limited sampling rate leads to lower sensitivity, and also the limitation of the inversion algorithm to the calculation results. Therefore, the spherical satellite has introduced the design of the pressure measurement sensor, and the obtained detection data may make up for the lower sensitivity of the precise orbit determination data in the inversion of atmospheric density in the future.

Table 1. The performances of the spherical satellite GPOD.

Pseudorange Accuracy	Carrier Phase Accuracy	Precise Orbit Determination Accuracy	Atmospheric Density Inversion Accuracy
≤30 cm	≤2 mm	≤5 cm	≤6.5%

2.2. Algorithm and Error Analysis Method

The inversion of atmospheric density by GPOD data follows the following principle. Firstly, the GNSS observation determines the orbit of the spherical satellite accurately to obtain the drag acceleration and the dimensionless atmospheric drag coefficient C_D along the orbit. Then, the atmospheric density at the orbit is inverted by the relationship between the drag acceleration and the atmospheric density. The relationship between the drag acceleration and the atmospheric density is as follows:

$$\ddot{r}_{Atm} = -\frac{1}{2}C_D \cdot Am \cdot \rho \cdot v_r^2 \tag{1}$$

where: ρ represents the atmospheric density; and \ddot{r}_{Atm} represents the drag acceleration along the velocity direction. The precision level of the drag acceleration calculated by the precise orbit determination method is nm/s^2 . v_r is the velocity of the satellite relative to the atmospheric ($V_r = V_{sat} + V_{atm}$). Am is the area-mass ratio on the windward. We assumed that the area-mass ratio Am and C_D on the windward of the spherical satellite are constant in any attitude.

Based on Equation (1), the equation for calculating atmospheric density is as follows:

$$\rho = -2 \cdot \ddot{r}_{Atm} / (C_D \cdot Am \cdot v_r^2) \tag{2}$$

In Figure 2a, the red curve indicates the atmospheric density value inverted from the GPOD data using Equation (2).

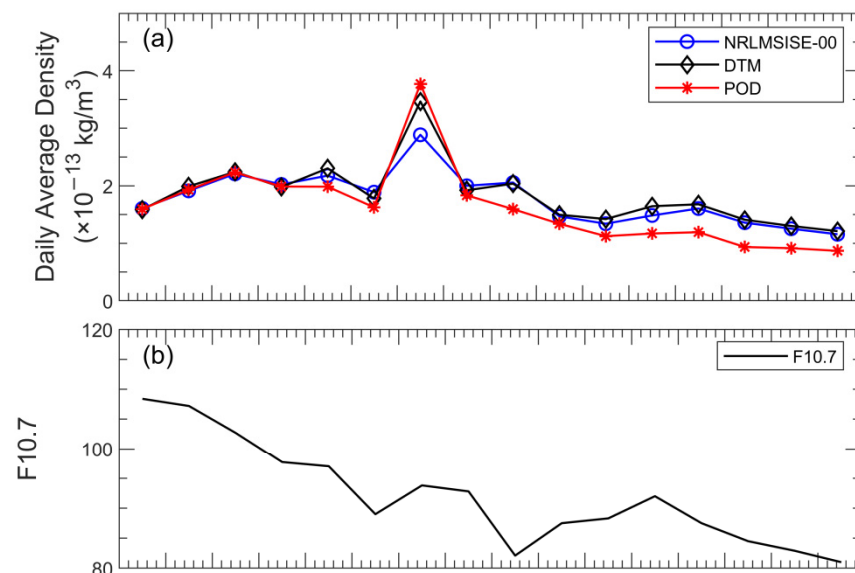


Figure 2. Cont.

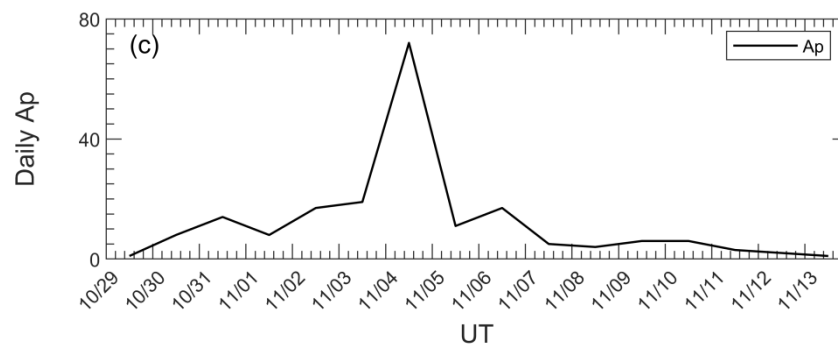


Figure 2. Variation of atmospheric density and spatial environmental indexes with time: (a) simulations and observations; (b) F10.7 index; (c) Ap index.

In this paper, we compared and analyzed the atmospheric density values calculated by NRLMSISE-00 and DTM94 models with the inversion results from the GPOD data. The deviation between the inversed atmospheric density by observation and the simulation results was evaluated by the distribution of the relative error, that is, the percentage of sampling points (confidence R) within the relative error range (error band μ). The equation for relative error is $R_i = \frac{\rho_{\text{model}}}{\rho_{\text{true}}} - 1$, where: ρ_{model} is the density value calculated by the models, and ρ_{true} is the density value inverted by the GPOD. If the total number of sampling points is N , then $\left| \frac{\rho_{\text{model}}}{\rho_{\text{true}}} - 1 \right| \leq \mu$; if the number of samples inside μ is M , then $R = \frac{M}{N}\%$.

3. Observational Results and Analysis

3.1. Comparison of Observations and Simulations

3.1.1. Daily Variations

Figure 2 indicates the profiles of the time-daily average atmospheric density by GPOD, time-daily average atmospheric density by DTM94 and NRLMSISE-00, time-solar activity index, and the time-geomagnetic disturbance index from 29 October to 13 November 2021.

1. Daily variations with solar activities

It can be found in Figure 2 that the simulations and the observations of atmospheric density had the same variation tendency with the solar activity index F10.7. The F10.7 index was 108.4 on 29 October 2021, and decreased to 81 on 13 November. On 29 October, the observations and simulations of DTM94 and NRLMSISE00 of the daily average atmospheric density were all $1.6 \times 10^{-13} \text{ kg/m}^3$. On 13 November, F10.7 index was 81, and the daily average atmospheric densities were $1.15 \times 10^{-13} \text{ kg/m}^3$, $1.21 \times 10^{-13} \text{ kg/m}^3$ and $8.7 \times 10^{-14} \text{ kg/m}^3$ respectively. Compared with those on 13 November, the atmospheric density on 29 October decreased, including the F10.7 index, which decreased by about 25.3%. The atmospheric density of DTM94 decreased by about 23.7%, and the atmospheric density of NRLMSISE-00 decreased by about 28.0%. The observed atmospheric density of GPOD decreased by about 45.0%.

2. Daily variations during the severe geomagnetic storm

During the severe geomagnetic storm, which occurred on 4 November 2021, the valley value of Dst index of the geomagnetic activity reached -105 nT on November 4, and Ap index increased from 19 on 3 November to 72 on 4 November; the simulations and the observations of atmospheric density both showed significant increases in the disturbance. As shown in Figure 2a, the daily average atmospheric density peaked on 4 November, and then plunged. From the third to the fourth, the measured value grew by about 132.0%, the simulation value of DTM94 grew by about 94.9%, and the simulation value of NRLMSISE-00 grew by about 52.8%. The simulation results growth of 37.1–79.9% is less than the observations. On 5 November, the simulations and the observations of atmospheric density both showed significant downward trends, and returned to the vicinity of the values on 3 November with a deviation of about 10%; compared with those on 4 November, the

observations decreased by 51.4%, the simulation results of DTM94 decreased by 44.5%, and the results of NRLMSISE-00 decreased by 30.7%. The decrease in the simulated values of 6.9–20.7% is less than the observed values.

3.1.2. Correlation Analysis

Considering the limited error in the simulation results of the atmospheric density models during the quiet period of the space environment, in Figure 3, we compared the atmospheric density inverted from the GPOD data with those calculated by DTM94 and NRLMSISE-00 on 29 October 2021 and 13 November 2021 with the relatively quietest geomagnetic disturbances in the week before and after the geomagnetic storm. Figure 3a,b indicate the correlation curves between the simulated values and the observed values. The x coordinate represents the observations, the y coordinate represents the simulations, and the dots are the GPOD measured average values of the atmosphere density on orbit. Figure 3c indicates the distribution curve of the relative error between the GPOD detections and the simulations. The x coordinate represents the error band, and the y coordinate represents the confidence. Figure 3 shows that during the relatively quiet period of the space environment, the correlations between the simulations of the two atmospheric density models and the GPOD observations were both better than 98%. The maximum error bands between the simulations and the observations were both 50%. A comparison between the error distributions of the two models relative to GPOD respectively is shown in Table 2, which indicates that the simulations of DTM94 better aligned with the observations. The correlation and error analysis showed that during the relatively quiet period of the space environment, there was a good consistency between the relative variation trend and the absolute value of the GPOD observations and the simulations.

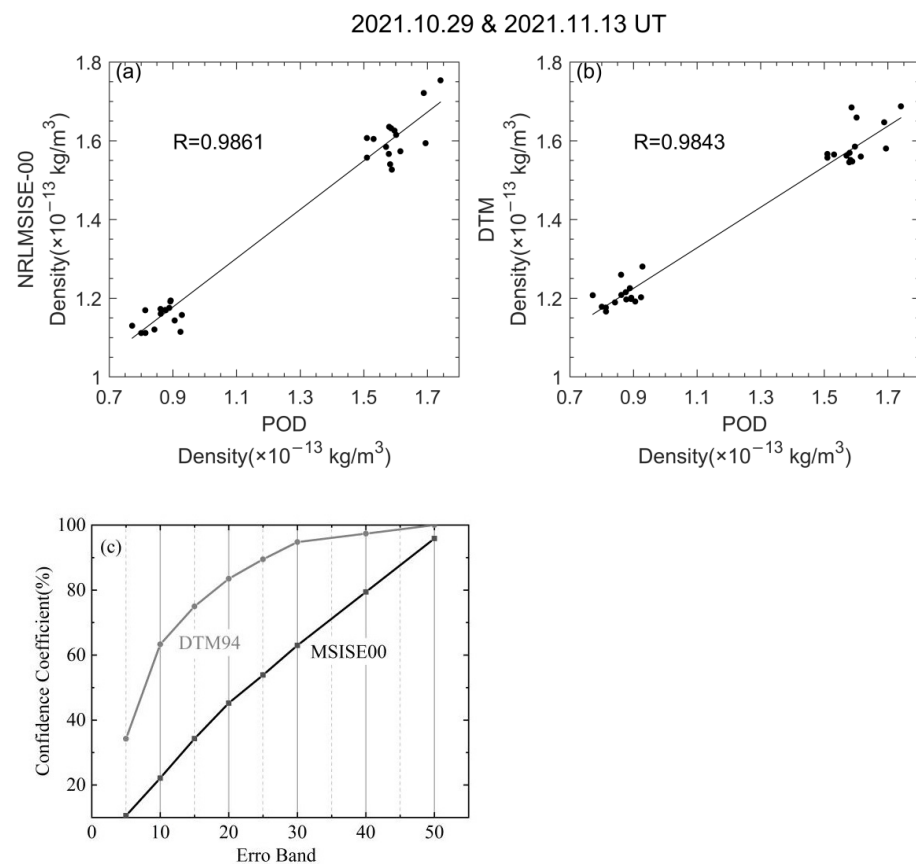


Figure 3. The correlation and error distribution between the simulations and the observations: (a) the correlation between the simulations by the NRLMSISE00 and the observations; (b) the correlation

between the simulations by the DTM94 and the observations; (c) the relative error distribution between the observations and the simulations.

Table 2. The error distributions of the two models relative to GPOD.

Model vs. GPOD	Error Band	Confidence Level
DTM94	±15%	75%
	±30%	95%
NRLMSISE-00	±15%	34%
	±30%	63%

The above analysis shows that during the observation, the time evolution curves of the calculated daily average values and the measured daily average values of atmospheric density followed the same trend. The atmospheric density fell with the decrease of the F10.7 index, but rose significantly during the severe geomagnetic storm. The variation trend of atmospheric density with space environmental disturbance conforms to the general mechanism. The simulations aligned better with the observations during the geomagnetic quiet period, which indicates the scientific validity of the observed data of the spherical satellite at an altitude of 520 km. During the severe geomagnetic storm, the relative variation of the simulations of atmospheric density with space environmental disturbances was weaker than that of the observations. This conforms to the argument by Doornbos et al. in 2008, that is, there was a large error in the model's response to environmental disturbances.

3.2. Atmosphere Density Variations during the Severe Geomagnetic Storm

The following is a preliminary analysis of the time evolution and the global distribution of the atmospheric density at different latitudes during the severe geomagnetic storm in the northern and southern hemispheres on the height of 520 km. Figure 4 shows the time and spatial distribution of the atmospheric density and its differences with time and geomagnetic latitude measured by GPOD from 3 November 2021 to 5 November 2021.

3.2.1. Time Evolution

As shown in Figure 4a, we compared the time variation of the absolute values of normalized atmospheric density high-latitude region at 70–90 degrees, the mid-latitude region at 40–60 degrees, and the equatorial low-latitude region at 0–10 degrees of the northern and southern hemispheres. The P1–P7 in the figure are P1 (3 November 2021 20:00), P2 (3 November 2021 22:00), P3 (4 November 2021 10:30), P4 (4 November 2021 12:30), P5 (4 November 2021 15:00), and P6 (5 November 2021 8:00). Where: P1 is the elevation time of the atmospheric density in the high-latitude and the mid-latitude of the northern and southern hemispheres, P2 is the elevation time in the equatorial low-latitude, P3 is the peak time in the high-latitude of the southern hemispheres, P4 is the peak time in the high-latitude and the mid-latitude of the northern hemisphere, P5 is about the peak time in the equatorial low-latitude and the mid-latitude of the southern hemisphere, and P6 is the time when the atmospheric density rising returns to the normal level.

When a geomagnetic storm occurs, the increase in atmospheric density starts from the mid- and high-latitude of the two hemispheres and gradually expands to the equatorial low-latitude. The atmospheric density in the south high-latitude and the north mid-high-latitude reached the peak after 16.5 h. The atmospheric density of the mid-latitude of the southern hemisphere reached the peak 18.5 h after the onset of the disturbance. The atmospheric density disturbance in the north high-latitude reached the peak with a lag of about 2 h compared with that in the south high-latitude. The atmospheric density disturbance in the equatorial low-latitude started almost simultaneously in the northern and southern hemispheres, and lagged behind the mid- and high-latitude of the two hemispheres by about 1 h. The atmospheric density in the equatorial low-latitude and the mid-latitude of the southern hemisphere reached their peaks almost simultaneously,

which is about 19 h from the onset of the atmospheric density disturbance in the equatorial low-latitude. As shown in Figure 4a-c, the onset and peaking time of atmospheric density disturbance was basically consistent with the onset and duration of $K_p > 4$, as well as the duration of the initial phase of the geomagnetic storm with increasing Dst index and the duration of the main phase with plunging Dst index. The global trend of atmospheric density disturbance recovered almost at the same time, with a total duration of about 36 h, which is ~ 18 h behind the time when the K_p index recovered to below 4, and it is in the recovery phase for the Dst index to gradually return to a steady state. After that, although the geomagnetic disturbance continued to around 7 November, the daily average atmospheric density returned to its pre-storm level.

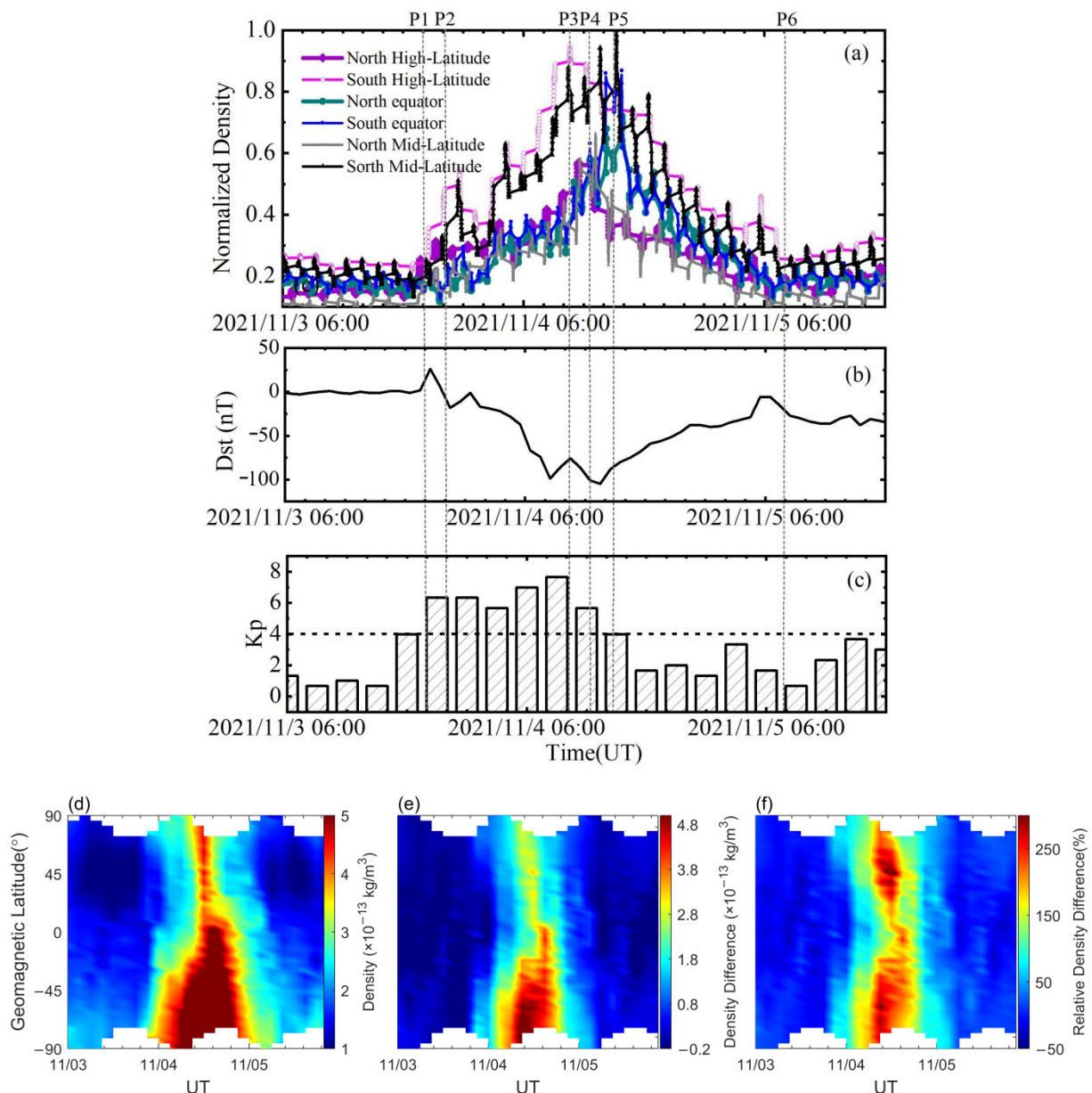


Figure 4. Time evolution and distribution of atmospheric density during the geomagnetic storm: (a) normalized atmospheric density at different geomagnetic latitudes; (b) Dst index; (c) K_p index; (d) absolute value of atmospheric density; (e) absolute change of atmospheric density; (f) relative variation of atmospheric density.

A comparison of the absolute peak values of atmospheric density in different latitudes of both hemispheres showed that for the southern hemisphere, the absolute peak values

of atmospheric density in the southern high-latitude were ~5.2% lower than those in the southern mid-latitude, and were ~31.5% higher than those in the southern equatorial low-latitude; for the northern hemisphere, the absolute peak values in the northern high-latitude were ~14.5% lower than those in the northern mid-latitude, and were ~34.6% lower than those in the northern equatorial low-latitude. A comparison between the northern and southern hemispheres concluded that the absolute peak value of atmospheric density in the southern high-latitude was ~66.8% higher than that in the northern high-latitude, the absolute peak value of atmospheric density in the equatorial low-latitude of the southern hemisphere was ~20.6% higher than that of the northern equatorial low-latitude, and the absolute peak value of the southern mid-latitude was ~33.5% higher than that in the northern mid-latitude.

3.2.2. Global Distributions

In Figure 4d–f, we compared the global distribution of the absolute values of atmospheric density during the severe geomagnetic storm, and the difference of ρ from the atmospheric density ρ_0 on quiet day relative to the same local solar time, that is, the absolute change $\Delta\rho_a$ and the relative variation $\Delta\rho_r$ of the atmospheric density, presented as $\Delta\rho_a = \rho - \rho_0$, and $\Delta\rho_r = \Delta\rho_a / \rho_0$. Where: ρ is the absolute value of atmospheric density during the storm from 3 November to 5 November 2021, and ρ_0 is the absolute value of atmospheric density during the relatively quiet period of the space environment on 29 October. The abovementioned equation may eliminate the effect of atmospheric density background changes [16]. $\Delta\rho_a$ represents the energy input during the storm [17], and $\Delta\rho_r$ may eliminate the deviation of the height effect [16].

Before and after the geomagnetic storm, the global distribution of atmospheric density showed a significant hemispheric asymmetry, that is, the southern hemisphere in summer had higher values than those in the northern hemisphere in winter, indicating a seasonal difference in atmospheric density at the altitude of 520 km during the relatively quiet period.

During a geomagnetic storm, mechanisms such as polar particle precipitation and Joule heating warm the upper polar atmosphere and drive large-scale wind fields, causing disturbances in global atmospheric density [18,19]. In addition to leading to the enhancement of upper atmosphere density, Joule heating can drive the variation of vertical wind in lower latitude by high-latitude enhanced wind circulation during geomagnetic storm, therefore causing the perturbation of density in low-mid-latitude regions [20,21]. During the geomagnetic storm, the atmospheric density ρ and $\Delta\rho_a$ near the altitude of 520 km showed a notable asymmetry between the northern and southern hemispheres, which were both significantly higher in the southern (summer) hemisphere than those in the northern (winter) hemisphere. Considering the fact that the southern hemisphere has stronger energy input than the northern hemisphere, the reason may be the asymmetry due to the combined effect of Joule heating and neutral winds. The prevailing summer-winter wind driven by solar heating promotes the density disturbance in summer hemisphere to the equator and limits the disturbance in the high-latitude of the winter hemisphere. In addition, the Joule heating in summer hemisphere was much higher than that in winter hemisphere, and even had a greater effect than particle precipitation [22,23], which conforms to the finding that the atmospheric density in the southern hemisphere in summer is more greatly enhanced than that in the northern hemisphere in winter; the equatorial atmospheric density peaks later than those in the mid- and high-latitude regions and the absolute value of atmospheric density in the equatorial low-latitude region of the northern hemisphere is lower than that of the southern hemisphere at the same latitude, but higher than that of the mid- and high-latitude regions of the northern hemisphere.

Figure 4f presents the observation of a bimodal distribution of the relative variation $\Delta\rho_r$ of atmospheric density in the northern and southern hemispheres at dawn and dusk during the severe geomagnetic storm with the altitude of 520 km. The distribution in the southern hemisphere was at geomagnetic latitudes $[-10^\circ, -90^\circ]$, and the distribution in

the northern hemisphere was at geomagnetic latitudes $[20^\circ, 90^\circ]$, indicating that around dawn and dusk during the geomagnetic storm, the large-scale circulation from the poles to the equator formed by atmospheric expansion exerted similar effects on the northern and southern hemispheres. The increase of $\Delta\rho_r$ in the southern hemisphere was wider than that in the northern hemisphere. The maximum values of $\Delta\rho_r$ in the northern and southern hemispheres both appeared in the mid-latitude regions, respectively about 308.0% at 58° south geomagnetic latitude around 9:00UT on 4 November and about 366.0% at 46° north geomagnetic latitude around 12:00UT on 4 November. The center of the low value of $\Delta\rho_r$ appeared near 10° geomagnetic latitude in the northern hemisphere. The overall structure follows a tendency of deviating from the magnetic equator and inclining toward the northern. This phenomenon that the overall atmospheric density disturbance rises in a larger range and $\Delta\rho_r$ reached peaks firstly in the southern hemisphere may be due to the faster disturbance of the prevailing wind circulation in the summer hemisphere than in the winter. $\Delta\rho_r$ appeared in the mid-latitude region, indicating that the increase in atmospheric density at dawn and dusk during the geomagnetic storm accounted for a larger proportion in the mid-latitude region. The maximum value of $\Delta\rho_r$ appeared in the northern hemisphere, which may be due to the low background value of atmospheric density in the northern hemisphere, leading to a greater impact of the disturbance on the background atmosphere.

4. Discussion and Conclusions

The GPOD loaded on the spherical experimental satellite is designed for the observation of the precise orbit determination data to invert the in-situ atmospheric density. The satellite was launched on 14 October 2021, marking the first time China performed in-situ measurement of atmospheric density from a satellite orbit at an altitude at 520 km. This paper introduced the spherical experimental satellite for the detection of atmospheric density, which inverted the in-situ atmospheric density on the polar orbit at an altitude of 520 km based on the drag acceleration calculated by the satellite precise orbit determination data obtained by GPOD, then analyzed the scientific validity of the atmosphere density data, and concluded the following major time evolution and global distribution at different latitudes in 520 km altitude of the dawn and dusk during the severe geomagnetic storm from 3 November 2021 to 5 November 2021:

1. The trend of the daily average atmospheric density with solar activity and geomagnetic disturbance conformed to the general mechanism of atmospheric density variation. During the quiet period, the observations were better aligned with the simulations, indicating the scientific validity of the detected data of the spherical satellite at an altitude of 520 km. During the severe geomagnetic storm, the relative variation of the simulations with space environmental disturbances was weaker than that of the observed data.
2. During the severe geomagnetic storm, the enhancement and recovery of the atmospheric density disturbance at an altitude of 520 km showed a severe correlation with the geomagnetic Kp index and Dst index. The significant increase in atmospheric density started simultaneously with $Kp > 4$ and the initial phase of the geomagnetic storm; the peaking of atmospheric density was almost at the same time with the returning of the Kp index to below 4 and the main phase of the geomagnetic storm. The recovery of atmospheric density disturbance to the pre-storm level was concurrent at different latitudes, and synchronized with the recovery of the geomagnetic storm. Despite continuous small geomagnetic disturbances after the recovery phase, the atmospheric density remained relatively stable.
3. Around the occurrence of the geomagnetic storm, a seasonal difference in atmospheric density ρ between the northern and southern hemispheres was observed by the dawn-dusk-orbit satellite at an altitude of 520 km. The atmospheric density in the southern hemisphere in the summer was higher than that in the northern hemisphere.

4. During the severe geomagnetic storm, the increase in atmospheric density observed by the dawn-dusk-orbit satellite at an altitude of 520 km started from the high-latitude of the two hemisphere and then extended to the equatorial low-latitude. The increasing in the southern hemisphere was greater than that in the northern hemisphere, and was quicker in propagating to the lower latitudes of the northern hemisphere, which indicated the presence of cross-equatorial flow in the total wind field, therefore limiting the equatorial flow in the northern hemisphere. The reason for this phenomenon is probably that the prevailing summer–winter wind driven by the solar heating caused the density disturbance in summer hemisphere to propagate towards the equator and limit the disturbance in the high-latitude of the winter hemisphere. In addition, Joule heating is more significant in the summer hemisphere than in the winter hemisphere, exerting even greater effects than particle precipitation, which led to an asymmetry of the disturbances increasing in the northern and southern hemispheres.
5. During the severe geomagnetic storm, the dawn-dusk-orbit satellite at an altitude of 520 km observed a nearly symmetrical growth of bimodal structure caused by the large-scale circulation from the two poles to the equator formed by the expansion of the polar atmosphere. The overall structure is inclined towards the northern hemisphere due to the inconsistent propagation velocity of the disturbance in the northern and southern hemispheres. During the geomagnetic storm, the increase in atmospheric density at dawn and dusk accounts for a larger proportion in the mid-latitude, so that the peak of the relative variation is located in the mid-latitude in both hemispheres; whereas the background of atmospheric density in the northern hemisphere is relatively low, and the disturbance has a greater impact on the ambient atmosphere, which led to the appearance of the maximum relative variation in the northern middle latitude.

As the pioneer for in-situ detection of orbital atmospheric density in a low-orbit microsatellite network, the spherical experimental satellite for obtaining the atmospheric density inverted from the GPOD data verified the feasibility of in-situ measurement of atmospheric density in a constellation network. The atmospheric density data can be used to analyze the short-term and long-term variations of the thermospheric density, to study the thermosphere–ionosphere coupling, to evaluate the accuracy of the atmospheric density models, determine precise orbit and orbit prediction, and to modify or establish the atmospheric density models, etc. In addition, studies on the detection results showed that the detection elements of the experimental satellite are insufficient. The research on the thermosphere–ionosphere coupling and the modeling of high-precision atmospheric density models require joint analysis and studies on the in-situ wind field of the thermospheric orbital atmosphere, orbital atmospheric temperature, composition, electron and ion density of the ionosphere, and other observational elements. These detection elements are expected to be included in the observation payload catalogue of the atmospheric density detection satellite constellation network in the future.

Author Contributions: Conceptualization ideas, X.W.; visualization, Y.J.; writing—original draft preparation, X.W. and Y.J.; data curation, Y.J. and X.M.; formal analysis, X.M.; writing—review and editing, D.D. and A.Z.; validation, D.D. and B.W.; resources, X.T., F.Y. and Y.C.; project administration, Y.S. and X.Z. All authors have read and agreed to the published version of the manuscript.

Funding: This research is supported by the Strategic Priority Research Program of the Chinese Academy of Sciences (Grant No. XDA17010303), the National Natural Science Foundation of China (NSFC, Grant No. 41204128), and the Foundation of Key Laboratory of National Defense Science and Technology, Chinese Academy of Sciences (CXJJ-22S031).

Data Availability Statement: The data are not publicly available due to independent launched QQ-Satellite current status is in an internal testing phase. The data presented in this study are available on request from the corresponding author. The polar-orbiting spherical experimental satellite datasets can be obtained from the repository provided by the National Space Science Center.

The NRLMSISE-00 empirical model is available at the CCMC website (<https://ccmc.gsfc.nasa.gov/>, accessed on 14 September 2021). The space weather indices including F10.7 and Ap are available at <http://celestrak.org/SpaceData/> (accessed on 10 November 2021). The space weather indices including Dst and Kp are available at the NASA OMNI website (<http://omniweb.gsfc.nasa.gov/>, accessed on 11 January 2022) or upon request from the corresponding author.

Acknowledgments: We appreciate the full support to our scientific research from the National Space Science Center, Chinese Academy of Sciences. The available data websites have promoted our work to a large extent. In particular, we give sincere thanks to the reviewers for valuable and helpful comments.

Conflicts of Interest: The authors declare no conflict of interest.

References

1. Taplay, B.D.; Schuts, B.E.; Born, G.H. *Statistical Orbit Determination*; Academic Press: Burlington, MA, USA, 2004; pp. 66–68. [[CrossRef](#)]
2. Qian, L.Y.; Solomon, S.C. Thermospheric density: An overview of temporal and spatial variations. *Space Sci. Rev.* **2012**, *168*, 147–173. [[CrossRef](#)]
3. Walterscheid, R.L. Solar Cycle Effects on the Upper Atmosphere: Implications for Satellite Drag. *J. Spacecr. Rockets* **1989**, *26*, 439–444. [[CrossRef](#)]
4. Smith, O.E.; Adelfang, S.I.; Smith, R.E. Neutral orbital altitude density effects on the International Space Station. *J. Spacecr. Rockets* **1997**, *34*, 817–823. [[CrossRef](#)]
5. Doornbos, E.; Klinkrad, H.; Visser, P. Use of two-line element data for thermosphere neutral density model calibration. *Adv. Space Res.* **2008**, *41*, 1115–1122. [[CrossRef](#)]
6. Reigber, C.; Lahr, H.; Schwintzer, X. CHAMP mission status. *Adv. Space Res.* **2002**, *30*, 129–134. [[CrossRef](#)]
7. Bruinsma, S.; Tamagnan, D.; Biancale, R. Atmospheric density derived from CHAMP/STAR accelerometer observations. *Planet. Space Sci.* **2004**, *52*, 297–312. [[CrossRef](#)]
8. Tapley, B.D.; Bettadpur, S.; Watkins, M.; Reigber, C. The Gravity Recovery and Climate Experiment: Mission overview and early results. *Geophys. Res. Lett.* **2004**, *31*, L09607. [[CrossRef](#)]
9. Nicholas, A.; Finne, T.; Galysh, I.; Davis, M.; Thomas, L.; Healy, L. The Atmospheric Neutral Density Experiment (ANDE). *Atmos. Sci. Technol.* **2009**, 138–141. Available online: https://www.researchgate.net/publication/235152249_The_Atmospheric_Neutral_Density_Experiment_ANDE (accessed on 14 September 2021).
10. Jun, Z.; Yingying, L.; Guanghui, L.; Bo, B.; Weijian, P.; Peijie, Z.; Xiaozhou, Y. QB50 Project and the Development of Cube Sat Technology in China. *Aerospace China* **2018**, *19*, 30–39.
11. Gill, E.; Sundaramoorthy, P.; Bouwmeester, J.; Zandbergen, B.; Reinhard, R. Formation flying within a constellation of nanosatellites: The QB50 mission. *Acta Astronaut.* **2013**, *82*, 110–117. [[CrossRef](#)]
12. Xingxing, L.; Keke, Z.; Xiangguang, M.; Wei, Z.; Qian, Z.; Xiaohong, Z.; Xin, L. Precise Orbit Determination for the FY-3C Satellite Using Onboard BDS and GPS Observations from 2013, 2015, and 2017. *Engineering* **2020**, *6*, 904–912. [[CrossRef](#)]
13. Yang, M.; Meng, X.; Sun, Y.; Du, Q.; Bai, W.; Wang, X.; Yang, G.; Liao, M.; Hu, P.; Tan, G. Preliminary Results of GPS-Based Precision Orbit Determination of FY-3E Satellite GNOS Dual-Antenna. *CSNC* **2022**, *910*, 209–219. [[CrossRef](#)]
14. Sun, Y.; Wang, B.; Meng, X.; Tang, X.; Yan, F.; Zhang, X.; Bai, W.; Du, Q.; Wang, X.; Cai, Y.; et al. Analysis of Orbital Atmospheric Density from QQ-Satellite Precision Orbits Based on GNSS Observations. *Remote Sens.* **2022**, *14*, 3873. [[CrossRef](#)]
15. Kuang, D.; Desai, S.; Sibthorpe, A.; Pi, X. Measuring atmospheric density using GPS–LEO tracking data. *Adv. Space Res.* **2014**, *53*, 243–256. [[CrossRef](#)]
16. Ercha, A.; Ridley, A.J.; Zhang, D.; Xiao, Z. Analyzing the hemispheric asymmetry in the thermospheric density response to geomagnetic storms. *J. Geophys. Res.* **2012**, *117*, 8317–8330. [[CrossRef](#)]
17. Burns, A.G.; Killeen, T.L.; Wang, W.; Roble, R.G. The solar-cycle-dependent response of the thermosphere to geomagnetic storms. *J. Atmos. Sol.-Terr. Phys.* **2004**, *66*, 1–14. [[CrossRef](#)]
18. Prolss, G.W.; Roemer, M.; Slowey, J.W. Dissipation of solar wind energy in the earth’s upper atmosphere: the geomagnetic activity effect. *Adv. Space Res.* **1988**, *8*, 215–261. [[CrossRef](#)]
19. Fuller-Rowell, T.J.; Codrescu, M.V.; Roble, R.G.; Richmond, A.D. How Does the Thermosphere and Ionosphere React to a Geomagnetic Storm? In *Magnetic Storms*; Tsurutani, B.T., Gonzalez, W.D., Kamide, Y., Arballo, J.K., Eds.; Geophysical Monograph Series: Washington, DC, USA, 1997; Volume 98, pp. 203–225. [[CrossRef](#)]
20. Li, J.; Wang, W.; Lu, J.; Yuan, T.; Yue, J.; Liu, X.; Zhang, K.; Burns, A.G.; Zhang, Y.; Li, Z. On the responses of mesosphere and lower thermosphere temperatures to geomagnetic storms at low and middle latitudes. *Geophys. Res. Lett.* **2018**, *45*, 10128–10137. [[CrossRef](#)]
21. Li, J.; Wang, W.; Lu, J.; Yue, J.; Burns, A.G.; Yuan, T.; Chen, X.; Dong, W. A modeling study of the responses of mesosphere and lower thermosphere winds to geomagnetic storms at middle latitudes. *J. Geophys. Res. Space Phys.* **2019**, *124*, 3666–3680. [[CrossRef](#)]

-
22. Bruinsma, S.; Forbes, J.M.; Nerem, R.S.; Zhang, X. Thermosphere density response to the 20–21 November 2003 solar and geomagnetic storm from CHAMP and GRACE accelerometer data. *J. Geophys. Res.* **2006**, *111*, 6303–6316. [[CrossRef](#)]
 23. Ahn, B.H.; Akasofu, S.I.; Kamide, Y. The Joule heat production rate and the particle energy injection rate as a function of the geomagnetic indices AE and AL. *J. Geophys. Res.* **1983**, *88*, 6275–6287. [[CrossRef](#)]